Journal of Computational Physics 228 (2009) 1541–1561

Contents lists available at ScienceDirect

Journal of Computational Physics

journal homepage: www.elsevier.com/locate/jcp

Discrete-element modeling of particulate aerosol flows

J.S. Marshall *

School of Engineering, The University of Vermont, 33 Colchecter Avenue, Burlington, Vermont 05405, United States

ARTICLE INFO

Article history:
Received 14 December 2005
Received in revised form 2 January 2008
Accepted 30 October 2008
Available online 11 November 2008

Keywords:
Particulate flow
Aerosols
Particle adhesion
Aggregation

ABSTRACT

A multiple-time step computational approach is presented for efficient discrete-element modeling of aerosol flows containing adhesive solid particles. Adhesive aerosol particulates are found in numerous dust and smoke contamination problems, including smoke particle transport in the lungs, particle clogging of heat exchangers in construction vehicles, industrial nanoparticle transport and filtration systems, and dust fouling of electronic systems and MEMS components. Dust fouling of equipment is of particular concern for potential human occupation on dusty planets, such as Mars. The discrete-element method presented in this paper can be used for prediction of aggregate structure and breakup, for prediction of the effect of aggregate formation on the bulk fluid flow, and for prediction of the effects of small-scale flow features (e.g., due to surface roughness or MEMS patterning) on the aggregate formation. After presentation of the overall computational structure, the forces and torques acting on the particles resulting from fluid motion, particle–particle collision, and adhesion under van der Waals forces are reviewed. The effect of various parameters of normal collision and adhesion of two particles are examined in detail. The method is then used to examine aggregate formation and particle clogging in pipe and channel flow.

1. Introduction

Fluid flows containing adhesive aerosol particles occur in a wide range of natural and engineering problems. Inhaled smoke particles with diameters ranging from 100 to 1000 nm can penetrate throughout the lungs, even down to the alveoli, leading to numerous respiratory diseases. Dust particle clogging is a cause of frequent system maintenance in many industrial systems. For instance, construction vehicles operating in dusty environments experience rapid dust clogging of the radiator and other heat exchangers associated with the vehicle cooling system, leading to the need for frequent vehicle down time. Dust fouling has long been a major maintenance concern for electronic equipment in general, where small dust particles adhering to electrical circuit boards can short out an electrical system. Similar concerns arise with MEMS systems, which are sensitive to small amounts of contamination and provide large surface area for dust adhesion. Ability to predict dust fouling is of particular importance for preparation for human and robotic exploration of dusty planets, such as Mars. Production of nanoparticles is of growing interest for various industrial applications, including use in anti-abrasion coatings, as fillers for advanced composite materials, and as coatings for advanced sensors, catalysts and battery electrodes. For flame-generated nanoparticle production processes in particular [28], processes such as particle transport, filtration, and dispersion all require an ability to predict aggregate formation in various fluid flows and its effect on the flow.

Computational models available for solution of flows with adhesive particles are quite varied in approach, but for the purposes of this introduction these models are divided into two general classes – population-based models and discrete-element models (DEM). Population-based models are typified by the Smoluchowski population balance equation [37], or

* Tel.: +1 802 656 3826; fax: +1 802 656 3358.
E-mail address: jeffm@cems.uvm.edu

0021-9991/$ - see front matter © 2008 Elsevier Inc. All rights reserved.
doi:10.1016/j.jcp.2008.10.035

Nomenclature

Roman letters

a	radius of contact region
a_0	equilibrium contact region radius (Eq. (38))
A_n	amplitude of particle cloud n (Eq. (14))
b	constant ($\cong$2.283)
$\mathbf{b}_{n,i}$	body force on grid cell i of fluid due to particle n (Eq. (12))
C	particle concentration field
c_{bulk}	bulk (or average) concentration
c_M	added mass coefficient (1/2 for a sphere)
C	constant (Eq. (50))
d	particle diameter
E	coefficient of restitution (Eq. (51))
E	effective elastic modulus of colliding particles (Eq. (16))
E_p	particle Young's modulus
F	friction factor
$f(\cdot,\cdot)$	weighting function for particle cloud
f_1, f_2, f_3	time step constants (less than unity)
$\mathbf{F}_a$	added mass force
$\mathbf{F}_A$	collision and adhesive force on particle
F_b	Basset history force
F_{crit}	critical sliding force
F_C	maximum particle adhesive force (Eq. (41))
$\mathbf{F}_d$	fluid drag force on particle
$\mathbf{F}_F$	fluid force on particle
$\mathbf{F}_g$	reduced gravitational force
$\mathbf{F}_\ell$	fluid lift force on particle
$\mathbf{F}_m$	Magnus force
F_n	normal collision/adhesion force
F_{nd}	dissipative part of normal collision/adhesion force
F_{ne}	elastic part of normal collision/adhesion force (Eq. (18))
$\mathbf{F}_p$	pressure gradient force
F_s	sliding force
$\mathbf{G}$	reduced gravitational acceleration
G	effective shear modulus of colliding particles (Eq. (16))
G_n	shear modulus of particle n
I	particle moment of inertia ($md^2/10$)
k_N	elastic stiffness (Eq. (20))
k_R	rolling stiffness
k_Q	torsional stiffness coefficient (Eq. (31))
k_T	tangential stiffness coefficient (Eq. (27))
K	stiffness coefficient (Eq. (21))
L	fluid characteristic length scale
m	particle mass
$\mathbf{M}_A$	collision and adhesive moment on particle
$\mathbf{M}_F$	fluid moment on particle (Eq. (1))
M_r	rolling torque on particle (Eq. (35))
M_t	twisting torque on particle
$M_{t,crit}$	critical twisting torque (Eq. (32))
$\mathbf{N}$	unit normal connecting the centroids of two particles
n_{PA}	aggregate size
$\bar{n}_{CP}$	average number of particles in a collision
N	number of particles
$N_a(\cdot)$	number of particles contained in an aggregate of a given size
N_A	number of aggregates
N_{CP}	total number of particles involved in collisions
r_n	radius of particle n
$\mathbf{r}_i$	vector from particle centroid to contact point ($r_i\mathbf{n}$)
R	effective radius of colliding particles (Eq. (16))
R_n	radius of particle cloud n

Re_F	fluid Reynolds number ($\rho_f LU/\mu$)
Re_P	particle Reynolds number ($\|\mathbf{v}-\mathbf{u}\|d/\nu$)
S	dimensionless shear parameter ($\omega L^2/\nu$)
St	Stokes number ($\rho_p d^2 U/18\mu L$)
t	time
$\mathbf{t}_R$	direction of particle rolling velocity ($\mathbf{v}_L/\|\mathbf{v}_L\|$)
$\mathbf{t}_S$	direction of particle sliding velocity ($\mathbf{v}_S/\|\mathbf{v}_S\|$)
T_{AP}	particle aerodynamic time scale ($T_F St$)
T_C	particle collision time scale ($d\left(\rho_p^2/E_p^2 U\right)^{1/5}$)
T_{CP}	particle convective time scale (d/U)
T_F	fluid convective time scale (L/U)
T_P	particle time scale ($\min(T_{AP}, T_{CP})$)
$\mathbf{U}$	fluid velocity at particle location
U	fluid characteristic velocity scale
$\mathbf{v}$	particle velocity
$\mathbf{v}_C$	particle surface velocity at contact point
$\mathbf{v}_L$	particle rolling velocity (Eq. (34))
$\mathbf{v}_R$	particle relative velocity at contact point
$\mathbf{v}_S$	particle slide velocity (Eq. (26))
V_i	volume of sub-grid cell opposite to node i(Fig. 2)
V	grid cell volume
W	collision rate ($d\delta/dt$)
w_0	measure of particle relative collision velocity
$\mathbf{X}$	position vector
$\mathbf{x}_n$	centroid position of particle n

Greek letters

α	coefficient of friction (Eq. (23))
α_L	coefficient of the lift force ($\|\boldsymbol{\omega}\|d/(2\|\mathbf{v}-\mathbf{u}\|)$)
β	exponent given by Eq. (4)
χ	fluid-to-particle density ratio (ρ_f/ρ_p)
δ_C	overlap at critical adhesive force (Eq. (41))
δ_N	normal overlap of particles (Eq. (17))
Δt	fluid time step
Δt_C	collision time step
Δt_P	particle time step
Δt	fluid time step
ε	dimensionless particle diameter (d/L)
ϕ	dimensionless adhesion coefficient (Eq. (55))
γ	adhesion surface potential
η_N	normal dissipation coefficient (Eq. (22))
η_R	rolling dissipation coefficient
η_Q	torsional dissipation coefficient (Eq. (31))
λ	elasticity parameter (Eq. (55))
μ	fluid viscosity
μ_f	friction coefficient
μ_R	rolling coefficient (Eq. (37))
ν	fluid kinematic viscosity (μ/ρ_f)
θ_{crit}	critical angular displacement due to rolling (ξ_{crit}/R)
ρ_f, ρ_p	fluid and particle densities
σ_n	Poisson's ratio of particle n
ω	vorticity magnitude
$\boldsymbol{\omega}$	fluid vorticity at particle location
$\boldsymbol{\Omega}$	angular rotation rate of particle
Ω_T	relative twisting rate (Eq. (28))
ξ	displacement of particle centroid due to rolling (Eq. (44))
ξ_{crit}	critical rolling displacement

Mathematical operators

d/dt	derivative following particle
D/Dt	derivative following fluid-particle (usual material derivative)
∇	del operator

Superscripts
^ dimensionless (Eq. (46))
* transformed (Eq. (48))

later variants of this equation [6,19,44], which relates the rate of change of the number of aggregates of a certain size, n_i, to various effects that lead to generation or elimination of aggregates of size n_i, resulting from aggregate collision and breakup processes. Expressions for each of these source/sink terms are developed using either deterministic physical models [37] or statistical arguments, such as those based on extensions of kinetic theory to granular media [23]. Population balance approaches have been sufficiently refined to provide reasonably accurate prediction of aggregate size distribution in different types of flow fields, but they cannot yield predictions of the micromechanics and microstructure of the aggregates or of their interactions with each other and with immersed surfaces in the flow. Of particular interest are situations where the flow length scale may approach the aggregate size and situations where aggregates become attached to solid surfaces in the flow, such as a channel wall or a fiber. Both of these types of situations are common in microfluidic flows.

The second general approach for simulation of adhesive particle flows is discrete-element models (DEM), wherein the transport and interactions of each particle are computationally followed. Discrete-element models have been used extensively for large-size particles, where adhesion effects are negligible, as well as for nanoscale particles, in which the particle size is compatible with the adhesion length scales, so the molecular dynamics approach can be directly applied. In between these two extremes is found a regime involving particles with diameter d much larger than the adhesion length scale but still small enough to exhibit significant particle adhesion, which for dry aerosols corresponds roughly to $0.1\ \mu\text{m} < d < 100\ \mu\text{m}$. Computational models for particles in this range exhibit high stiffness, due to the large difference between the several time scales involved in the problem, ranging from the fluid advection time at the upper end to the time associated with particle adhesion forces at the lower end. A second challenge for models of this sort is the necessity to include in the computational model a wide range of forces and torques acting on the particles, due to both fluid flow and to collision events. Among the latter include the elastic and dissipative normal forces and the resistance from particle sliding, twisting and rolling motions. Many of the collision forces and torques are significantly affected by the adhesive force. In development of discrete-element models for adhesive particles, both the physical and computational modeling issues must be accounted for in tandem, since in many cases models exist for these various forces which, while accurate, would not be computational feasible for large numbers of particles. At the same time, the interests of computational efficiency leads some studies of adhesive particle flows to neglect effects, such as rolling resistance, which play a critical role in the aggregate dynamics and breakup.

An early DEM study for adhesive particle flows is presented by Mikami et al. [30], who consider cohesive powders subject to liquid bridging force. Dominik and Tielens [13] present a DEM with van der Waals forces [42], which they use to examine impact of ice particles in space. Many of these previous DEM studies for adhesive particle flows report results only for two-dimensional flows and with relatively small number of particles, due in large part to the time step restriction caused by the stiffness of the governing equations for particle adhesion force. One option to partially circumvent the problem of a small time step was proposed by Weber et al. [43], who replace the van der Waals potential with a square-well potential and use a hard-sphere model for the particle collisions, in which particles collide both with their respective surfaces and with the outer surface of the cohesive energy well surrounding each particle. The minimum time step for this method is on the order of the time required for the particle surface to cross the thickness of the adhesive energy well.

The present paper presents a computational discrete-element model for efficient, physically-accurate evolution of particulate aerosol flows with micron-size particles. The model involves both physical and computational modeling components, which are developed to be true to the physics of collision- and fluid-induced forces and torques acting on the particles, while at the same time consistent with the demands of rapid computation for large numbers of particles. The method is presented for small particles immersed in a fluid flow subject to van der Waals adhesive forces, but it has been extended in on-going work for other adhesive forces, including liquid bridging and ligand-receptor bonding. Computationally efficient models for the various forces and torques on the particles due to fluid flow effects and to collision and adhesion with other particles are critically reviewed. The model is then applied to examine aggregate formation for pipe and channel flows subject to different conditions, with investigations focusing on the role of the channel walls on particle capture and the aggregate formation process.

The structure of the computational algorithm is described in Section 2. Fluid-particle coupling is described in Section 3. The particle forces and torques resulting from collisions are reviewed in Section 4, including normal impact force and resistance for sliding, twisting and rolling motions. Modifications to the collision forces and torques arising from van der Waals adhesion are discussed in Section 5. The behavior of the computational model is examined for two particle collisions in Section 6. The method is applied in Section 7 to examine the process of particle aggregate formation in pipe and channel flows. Conclusions are given in Section 8.

2. Structure of computational model

In a discrete-element method, the particle velocity $\mathbf{v}$ and rotation rate $\boldsymbol{\Omega}$ are obtained by solution of the particle linear and angular momentum equations, given by

$$m\frac{d\mathbf{v}}{dt} = \mathbf{F}_F + \mathbf{F}_A, \quad I\frac{d\boldsymbol{\Omega}}{dt} = \mathbf{M}_F + \mathbf{M}_A \tag{1}$$

where m is the particle mass, d is the particle diameter, $I = (1/10)md^2$ is the particle momentum of inertia, and d/dt is the derivative following a moving particle. The forces acting on the particle are the fluid force ($\mathbf{F}_F$) and the elastic collision force and van der Waals adhesion force, which are together denoted as $\mathbf{F}_A$. In the angular momentum equation, $\mathbf{M}_F$ and $\mathbf{M}_A$ denote the corresponding fluid torque and the sum of the collision and van der Waals adhesion torques on the particle. While for dilute particle flows it is common to only compute particle translation, for colliding particles the rotation rate has a strong effect on the tangential particle forces. Formation of particle aggregates is found to be particularly sensitive to accurate evolution of the particle rotation rate.

The particle transport calculation exhibits a number of different time scales. Typically the largest time scale is that associated with the fluid flow. If L and U denote characteristic macroscopic length and velocity scales of the flow field and d denotes the typical particle diameter, the convection time scales of the fluid and the particles, $T_F = L/U$ and $T_{CP} = d/U$, are referred to here as the *fluid time scale* and the *particle convective time scale*. An alternative particle time scale is given by the *particle aerodynamic response time*, $T_{AP} \equiv T_F St$, where the Stokes number St is defined by $St \equiv \rho_p d^2 U/18\,\mu L = \varepsilon^2 Re_F/(18\chi)$. Here $\chi \equiv \rho_f/\rho_p$ is the fluid-to-particle phase density ratio, $\varepsilon \equiv d/L$ is the dimensionless particle diameter, and $Re_F \equiv \rho_f LU/\mu$ is the fluid macroscopic Reynolds number. Resolution of the particle response to fluid forces requires that the computation resolve the particle motion on the aerodynamic time scale, whereas identification and resolution of particle collisions requires that the particle motion be resolved on the particle convective time scale. We therefore set the *particle time scale* $T_P = \min(T_{CP}, T_{AP})$. The time scale that characterizes the elastic response of a particle when it collides with another particle, called the *collision time scale*, is given by $T_C = d\left(\rho_p^2/E_p^2 U\right)^{1/5}$, where E_p is the particle Young's modulus [41].

As a typical example, we consider dust particles in air. For dust particle diameter of 10 μm, density ratio of $\chi \cong 4 \times 10^{-4}$, and fluid length and velocity scales of 1 cm and 1 m/s, respectively, the corresponding Stokes number is $St = 0.1$. The fluid time scale is $T_F \cong 0.01$ s, and the particle convective and aerodynamic time scales are $T_{CP} \cong 10^{-5}$ s and $T_{AP} \cong 10^{-3}$ s, respectively. Setting $T_P = T_{CP}$, we obtain the particle-to-fluid time scale ratio as $T_P/T_F = 0.001$. Using an elastic modulus for quartz of $E_p \cong 70$ GPa, the collision time scale is obtained as $T_C \cong 10^{-8}$ s, giving $T_C/T_P = 0.001$, or six orders of magnitude difference between the fluid and collision time scales.

The computational structure is designed with a multiple-time step framework, such that the different computational tasks are performed with different frequencies depending on the time scale with which they change. Three of the major computational tasks are listed below:

(A) Fluid flow calculation: If the fluid flow is unsteady, we need to advance the flow field in time in order to compute the fluid forces on the particles. A two-way interaction approach is employed that accounts for particle forces on the fluid flow using a distributed body force, which is obtained by an averaging procedure over the particles.

(B) *Local list formation*: Many computational operations require calculation of the interaction of a particle with neighboring particles, including particle–particle collision and adhesion forces and modification of drag force due to particle crowding. To facilitate such calculations, we store a list for each particle identifying neighboring particles, referred to as the "local list". Local list formation is accelerated by first sorting the particles into a Cartesian grid, with grid size set equal to the typical search radius for the local list. The local list for each particle is determined by sorting particles in the grid cell containing the given particle and from particles in neighboring grid cells, taking into account periodic boundary conditions where appropriate. For later convenience, the local list of each particle is sorted using a heapsort algorithm such that the closest particles are listed first.

(C) Fluid forces on particles: Computation of the fluid forces acting on a particle requires knowledge of the fluid velocity at the particle center location, which must be obtained from interpolation from the grid used to store the fluid variables. The fluid force on a particle changes due both to change in the flow field and change in the particle location.

(D) *Identification of colliding particles:* It is useful to identify particle pairs that have collided during the time step in order to account for collision forces on these particles.

(E) Collision and adhesion forces on particles: We employ a "soft-sphere" approach popular in the granular flow literature (e.g., [41]) to compute the forces on each particle due to collision with nearby particles or container walls. As described in Section 5, the collision forces are modified here to account for the particle adhesion force.

The computation is performed using three distinct time steps listed below:

$$\begin{aligned}&\text{Fluid Time Step}: \quad \Delta t = f_1 T_F,\\ &\text{Particle Time Step}: \quad \Delta t_p = f_2 T_P,\\ &\text{Collision Time Step}: \quad \Delta t_C = f_3 T_C,\end{aligned}$$

where f_1, f_2, f_3 are constants with values much less than unity. Because the time scales associated with the problem are so different, we perform the different computational tasks listed above with a frequency associated with one of these time scales. A flow chart indicating the structure of the computational scheme is given in Fig. 1. The local list construction, which

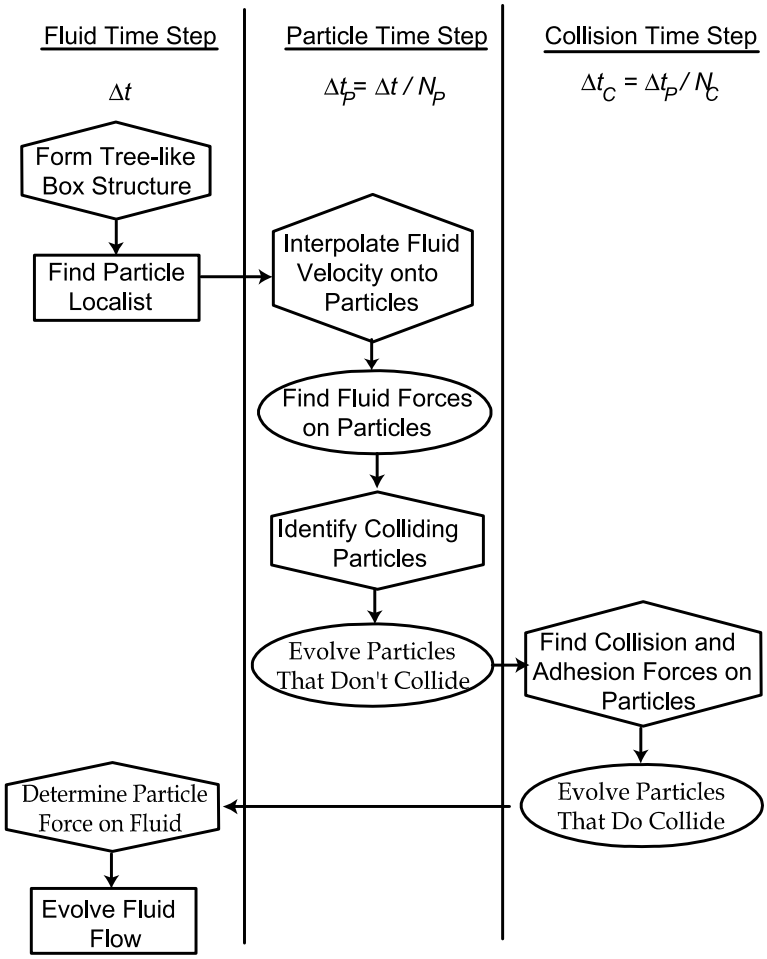

Fig. 1. Flow chart showing the structure of the computational algorithm, indicating major tasks that are performed on each of the three time steps. The most time-consuming tasks are enclosed in a rectangle, moderately timer-consuming tasks are enclosed in a hexagon, and less time-consuming tasks are enclosed in an oval.

tends to be time-consuming, is performed on the frequency of the fluid time scale. This list must therefore be made sufficiently large to encompass the different neighboring particles that each particle will see as it is advected over the time step Δt, but not so large as to lead to excessive computational time or storage requirements. Calculation of the fluid force on the particles is performed at the frequency of the particle time step, due to the need to account for the change in these forces as the particles move. We also store all previous particle collisions from the last time step into an array for each particle, and then add to this array an estimate of any new collisions that will occur during the particle time step. Particles that do not collide during the particle time step are advected with time step Δt_P. Particles that do collide during the particle time step are advected instead with the smaller collision time step Δt_C in order to properly account for the more rapid time variation of the collision and adhesion forces on the particle.

3. Fluid forces and torques

Fluid forces on the particles include drag, lift, pressure gradient (or buoyancy), gravity, added mass force, and Magnus force. The particle Reynolds number, $Re_P \equiv |\mathbf{v} - \mathbf{u}|d/\nu$ where $\mathbf{u}$ is the fluid velocity at the particle location and $\nu = \mu/\rho_f$ is the fluid kinematic viscosity, and the dimensionless particle diameter $\varepsilon \equiv d/L$ are both assumed to be much smaller than unity.

For small particles, the dominant fluid force is usually the drag force $\mathbf{F}_d$, given by

$$\mathbf{F}_d = -3\pi d\mu(\mathbf{v} - \mathbf{u})f. \tag{2}$$

The Stokes drag solution for an isolated sphere is recovered for friction factor $f = 1$. The correlation of Di Felice [11] is used to correct friction factor to account for particle crowding in non-dilute flows, giving

$$f = (1-c)^{-\beta}, \tag{3}$$

where $c(\mathbf{x},t)$ is the local particle concentration (i.e., the ratio of the particle volume to the fluid volume in a small region around the particle) and β is given by

$$\beta = 3.7 - 0.65\exp\left(-\frac{1}{2}[1.5 - \ln(Re_P)]^2\right). \tag{4}$$

The reduced gravity force $\mathbf{F}_g$ is

$$\mathbf{F}_g = m(1-\chi)\mathbf{g}, \tag{5}$$

where $\mathbf{g}$ is the gravitational acceleration vector. The gravity force is important even for small particles over sufficiently long time periods, unless the particle size is so small that the particles can be suspended indefinitely by Brownian motion. The pressure gradient force $\mathbf{F}_p$, due to the acceleration of the external flow past the particle, is

$$\mathbf{F}_p = \chi m \frac{D\mathbf{u}}{Dt}, \tag{6}$$

where D/Dt denotes the rate of change with time following a fluid particle, such that

$$\frac{D\mathbf{u}}{Dt} = \frac{d\mathbf{u}}{dt} - [(\mathbf{v}-\mathbf{u})\cdot\nabla]\mathbf{u}. \tag{7}$$

The added mass force $\mathbf{F}_a$ is given by

$$\mathbf{F}_a = -c_M \chi m\left(\frac{d\mathbf{v}}{dt} - \frac{d\mathbf{u}}{dt}\right), \tag{8}$$

where the added mass coefficient for a sphere is $c_M = 1/2$. The ratio F_p(or F_a)$/F_d \approx O(\chi)$, so these forces are generally small when the particle density is much greater than the fluid density.

A particle placed in a shear flow exhibits a lift force $\mathbf{F}_\ell$ in the direction normal to the direction of the flow. If the particle is assumed to rotate at the same rate as the local rotation rate of fluid particles, the lift force solution of Saffman [33,34] can be written as

$$\mathbf{F}_\ell = -2.18\chi m \frac{(\mathbf{v}-\mathbf{u})\times\boldsymbol{\omega}}{Re_P^{1/2}\alpha_L^{1/2}}, \tag{9}$$

where $\alpha_L \equiv |\boldsymbol{\omega}|d/(2|\mathbf{v}-\mathbf{u}|)$. The ratio $F_\ell/F_d = O(\varepsilon S^{1/2})$, where $S \equiv \omega L^2/\nu$ is a dimensionless shear parameter. For small particles ($\varepsilon \ll 1$), the lift force is generally small compared to drag except in regions of very large vorticity. We note that the Basset history force F_b is neglected in this model since for small particles the ratio of Basset force to drag scales as $F_b/F_d \cong Re_p^{1/2} \ll 1$. A detailed discussion of the effects of Basset force on particle motion is given by Druzhinin and Ostrovsky [14].

When the particle rotation rate differs from that of the surrounding fluid, an additional force (called the Magnus force) is exerted on the particles, given by

$$\mathbf{F}_m = -\frac{3}{4}\chi m\left(\frac{1}{2}\boldsymbol{\omega} - \boldsymbol{\Omega}\right)\times(\mathbf{v}-\mathbf{u}). \tag{10}$$

Assuming that the differential rotation occurs through the particle inertia under the fluid-induced torque, and using the scaling $|\mathbf{v}-\mathbf{u}|/U = O(St)$ developed by Crowe et al. [9], the ratio of Magnus force to drag is given by $F_m/F_d = O(\varepsilon S\, St)$. Particle collision in the presence of sliding resistance leads to much larger relative rotation rate between the particle and surrounding fluid, so that the Magnus force is typically greater than this estimate in the presence of collisions. The corresponding torque on the particle due to local fluid rotation is given by [9]

$$\mathbf{M}_F = \pi\mu d^3\left(\frac{1}{2}\boldsymbol{\omega} - \boldsymbol{\Omega}\right). \tag{11}$$

In additional to the forces listed above, it often necessary to include a random force acting on the particles. For very small particles (less than a micron diameter), this random force results from the Brownian motion induced by individual molecular collisions with the particle. For turbulent flows, a random force is often used to model effects of sub-grid-scale turbulence on dispersion of the particles. A review of random force models for particulate flows is given by Crowe et al. [9].

The particles exert a body force on the fluid flow, which must be accounted for cases with significant particle mass loading [9]. This body force is computed by determining the fluid grid cell in which each particle lies and distributing the force $-(\mathbf{F}_F - \mathbf{F}_g)_n$ on the fluid imposed by particle n onto the surrounding grid nodal points by the equation

$$\mathbf{b}_{n,i} = -(\mathbf{F}_F - \mathbf{F}_g)_n (V_i/V). \tag{12}$$

where V_i is the volume of the sub-grid cell opposite to node i, as shown in Fig. 2, and V is the total grid cell volume. The value of the body force at grid i is obtained by summing over the contributions from all particles contained in grid cells connected to node i. The Navier–Stokes equations are modified by the presence of two-way coupling with the particulate phase as

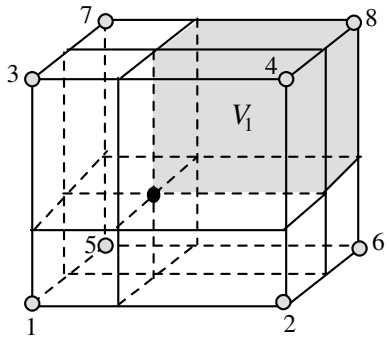

Fig. 2. Schematic illustrating the volume partitioning used to distribute particle forces onto the fluid grid. The volume V_1 opposite node 1 is shaded in gray.

$$\frac{\partial}{\partial t}(c_v\rho_f) + \nabla\cdot(c_v\rho_f\mathbf{u}) = 0 \tag{13a}$$

$$\frac{\partial}{\partial t}(c_v\rho_f u_i) + \frac{\partial}{\partial x_j}(c_v\rho_f u_i u_j) = \frac{\partial}{\partial x_j}\left[c_v\mu\left(\frac{\partial u_i}{\partial x_j}+\frac{\partial u_j}{\partial x_i}\right)\right] - c_v\frac{\partial p}{\partial x_i} - b_i. \tag{13b}$$

where $c_v \equiv 1\text{-}c$ is the voidage fraction.

The particle concentration field is used both in the Navier–Stokes equation (13) and in the correction (3) to the drag force, as well as in post-processing. Particle concentration can be obtained by counting the number of particles in each fluid grid cell; however, this approach tends to be noisy, particularly as the grid increment is made progressively smaller. We employ an alternative method for computing particle concentration using a variant of the particle cloud approach [29]. In this approach, we let the contribution to the continuous particle concentration field from each particle be distributed as a "cloud" around the particle center location as determined by a weighting function $f(\mathbf{x}-\mathbf{x}_n,R_n)$, such that the integral of f over all space equals unity and R_n is a length scale called the cloud radius. We choose a Gaussian function for f of the form

$$f(\mathbf{x}-\mathbf{x}_n,R_n) = \frac{2}{3\pi R_n^3}\exp[-|\mathbf{x}-\mathbf{x}_n|^2/R_n^2]. \tag{14}$$

The concentration $c(\mathbf{x},t)$ at a point $\mathbf{x}$ is obtained by summing over the contributions of the nearby particle clouds as

$$c(\mathbf{x},t) = \sum_{n=1}^{N} A_n f(\mathbf{x}-\mathbf{x}_n,R_n), \tag{15}$$

where the cloud amplitude A_n and cloud radius R_n are held constant for each computational particle. The cloud amplitude is equal to the particle volume, or $A_n = (\pi/6)d_n^3$, such that the integral of the concentration field over all space equals the sum of all the particle amplitudes, or the total volume occupied by the particles.

4. Collision forces with no adhesion

The forces and torques acting on the particles are decomposed into four parts: that acting along the line normal to the particles centers and the resistance from sliding, twisting, and rolling of one particle over another (Fig. 3). The normal force acts in the direction of the unit vector $\mathbf{n}$ which points tangent to the line connecting the centers of the two particles, denoted by i and j, such that $\mathbf{n} = (\mathbf{x}_j-\mathbf{x}_i)/|\mathbf{x}_j-\mathbf{x}_i|$. Since for spherical particles the normal force acts in the direction $\mathbf{n}$ passing through the particle centroids, it exerts no torque on the particles. The sliding resistance acts in a direction $\mathbf{t}_S$, corresponding to the direction of relative motion of the particle surfaces at the contact point projected onto the contact plane (the plane orthogonal to $\mathbf{n}$). The sliding resistance also imposes a torque on the particle in the $\mathbf{n}\times\mathbf{t}_S$ direction. The twisting resistance exerts a moment on the particle in the $\mathbf{n}$ direction, normal to the contact plane. The rolling resistance exerts a torque on the particle in the $\mathbf{t}_R\times\mathbf{n}$ direction, where $\mathbf{t}_R$ is the direction of the "rolling" velocity, which we define later in this section. The total collision and adhesion force and torque fields on particle i can then be written as

$$\mathbf{F}_A = F_n\mathbf{n} + F_s\mathbf{t}_S, \quad \mathbf{M}_A = r_i F_s(\mathbf{n}\times\mathbf{t}_S) + M_r(\mathbf{t}_R\times\mathbf{n}) + M_t\mathbf{n}, \tag{16}$$

where r_i is the radius of particle i.

4.1. Normal force

The normal force (F_n) is composed of the sum of a part (F_{ne}) due to the elastic deformation of the particles and a second part (F_{nd}) due to energy losses during the normal particle impact, which for small relative particle speeds result mainly from elastic wave propagation on the particles [21]. We consider two particles with radii r_i and r_j, elastic moduli E_i and E_j, Poisson

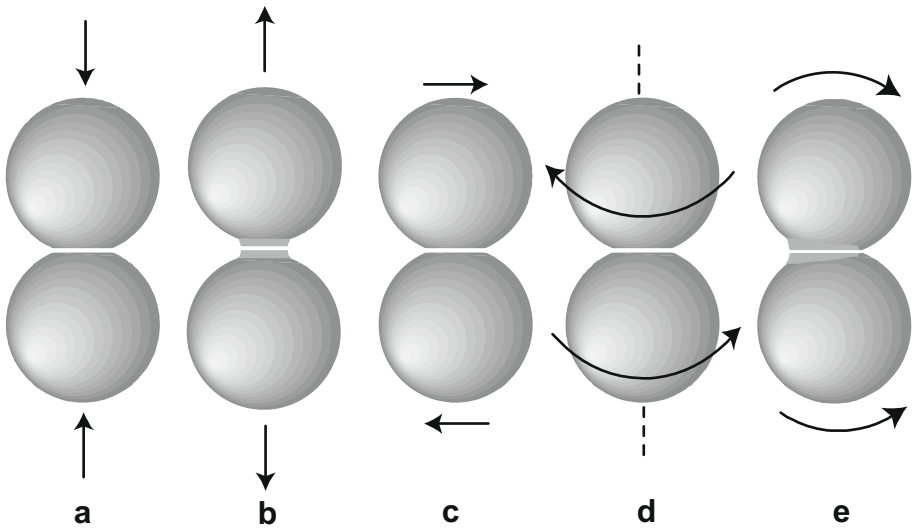

Fig. 3. Modes of particle interaction: (a) normal impact, (b) necking in normal extension, (c) shearing, (d) twisting, and (e) rolling.

ratios σ_i and σ_j, and shear moduli $G_i = E_i/2(1+\sigma_i)$ and $G_j = E_j/2(1+\sigma_j)$. An effective particle radius R and effective elastic and shear moduli E and G are defined by

$$\frac{1}{R} \equiv \frac{1}{r_i} + \frac{1}{r_j}, \quad \frac{1}{E} \equiv \frac{1-\sigma_i^2}{E_i} + \frac{1-\sigma_j^2}{E_j}, \quad \frac{1}{G} \equiv \frac{2-\sigma_i}{G_i} + \frac{2-\sigma_j}{G_j}. \tag{17}$$

The particle normal overlap δ_N is defined by

$$\delta_N = r_i + r_j - |\mathbf{x}_i - \mathbf{x}_j|, \tag{18}$$

where $\mathbf{x}_i$ and $\mathbf{x}_j$ denote the centroid positions of the two particles. Expressions for the elastic response F_{ne} and the radius $a(t)$ of the flattened contact region was obtained in the classic paper by Hertz [17] as

$$F_{ne} = -k_N \delta_N = -K \delta_N^{3/2}, \tag{19}$$

and

$$a^2 = R\delta_N. \tag{20}$$

The elastic stiffness k_N can be expressed in terms of the contact region radius as

$$k_N = \frac{4}{3} E a(t), \tag{21}$$

such that the stiffness coefficient K is given by

$$K = \frac{4}{3} E \sqrt{R}. \tag{22}$$

The dissipation force F_{nd} is given by

$$F_{nd} = -\eta_N \mathbf{v}_R \cdot \mathbf{n}, \tag{23}$$

where $\mathbf{v}_{C,i} = \mathbf{v}_i + \boldsymbol{\Omega}_i \times \mathbf{r}_i$ is the surface velocity of particle i at the contact point, $\mathbf{r}_i = r_i\mathbf{n}$ and $\mathbf{r}_j = -r_j\mathbf{n}$ are the vectors from the particle centroids to the contact point, $\mathbf{v}_R = \mathbf{v}_{Ci} - \mathbf{v}_{Cj}$ is the relative particle surface velocity at the contact point, and η_N is the normal friction coefficient. Cundall and Strack [10] and Tsuji et al. [41] propose expressions for η_N in which $\eta_N \propto (mk_N)^{1/2}$, where $k_N = F_{ne}/\delta_N$ is the normal stiffness coefficient. Tsuji et al. [41] propose that the damping coefficient is related to the coefficient of restitution if η_N is assumed to have the form

$$\eta_N = \alpha (mk_N)^{1/2}, \tag{24}$$

where α is a coefficient of friction that is written as a function of the restitution coefficient of the particles (see Section 7). Other expressions for η_N have also been proposed. For instance, Brilliantov et al. [5] examine the damping produced by collisions of two viscoelastic particles and propose an expression for normal damping coefficient where $\eta_N \propto a$, whereas substitution of (21) into (24) gives $\eta_N \propto a^{1/2}$. Since most of the literature on normal particle collision reports results in terms

of the restitution coefficient, it is often convenient to use the expression (24) for η_N and then account for effects such as viscous fluid damping [3] and material viscoelastic or wave propagation losses through modification of the restitution coefficient. For the small particles in the size range under consideration in this paper, most of the dissipation is due to fluid friction within the lubrication layer separating the particles, where the Stokes number is sufficiently low that the restitution coefficient is effectively zero.

4.2. Sliding resistance

We adopt a spring-dashpot-slider model for the sliding resistance proposed by Cundall and Strack [10], which is shown schematically in Fig. 4. In this model, the tangential sliding force F_s is first absorbed by the spring and dashpot until its magnitude reaches a critical value $F_{crit} = \mu_f |F_n|$. The friction coefficient μ_f has a typical value of about 0.3 for dry surfaces, but can be substantially reduced by the presence of the fluid within the contact region, particularly for smooth particle surfaces. If $|F_s| > F_{crit}$, then the particle surfaces will slip (as represented by the slider in Fig. 4) and the friction coefficient will be given by the modified Amonton friction expression

$$F_s = -F_{crit}. \tag{25}$$

For the subcritical case $|F_s| < F_{crit}$, the sliding resistance due to the spring and dashpot for particle i yields [8,41]

$$F_s = -k_T \left(\int_{t_0}^{t} \mathbf{v}_S(\xi) d\xi \right) \cdot \mathbf{t}_S - \eta_T \mathbf{v}_S \cdot \mathbf{t}_S, \tag{26}$$

where the slip velocity $\mathbf{v}_S(t)$ is the tangent projection of $\mathbf{v}_R$ to the particle surface at the contact point, or

$$\mathbf{v}_S = \mathbf{v}_R - (\mathbf{v}_R \cdot \mathbf{n})\mathbf{n} \tag{27}$$

and the slip direction is $\mathbf{t}_S = \mathbf{v}_S / |\mathbf{v}_S|$. The first term on the right-hand side of (26) is an elastic spring and the second term is viscous friction. The time integral in the first term gives the tangential elastic displacement of the material before slipping sets in, where t_0 is the time of initial particle impact.

An expression for the tangential stiffness coefficient k_T is derived by Mindlin [31]. Rewriting this expression in terms of the contact region radius $a(t)$ gives

$$k_T = 8Ga(t). \tag{28}$$

Tsuji et al. [41] assume that the tangential dissipation coefficient is of the same order as the normal viscous damping coefficient, so that lacking further information they set $\eta_T = \eta_N$. Other investigators in granular flows omit the last term in (26), which reduces to the common stick-slip friction model.

4.3. Twisting resistance

Twisting occurs when the two colliding particles have different rotation rate in the direction $\mathbf{n}$ (Fig. 3(d)). The relative twisting rate Ω_T is defined by

$$\Omega_T = (\boldsymbol{\Omega}_i - \boldsymbol{\Omega}_j) \cdot \mathbf{n}, \tag{29}$$

In analogy to the friction model (26) used for sliding, we propose a twisting resistance expression of the form

$$M_t = -k_Q \int_{t_0}^{t} \Omega_T(\tau) d\tau - \eta_Q \Omega_T. \tag{30}$$

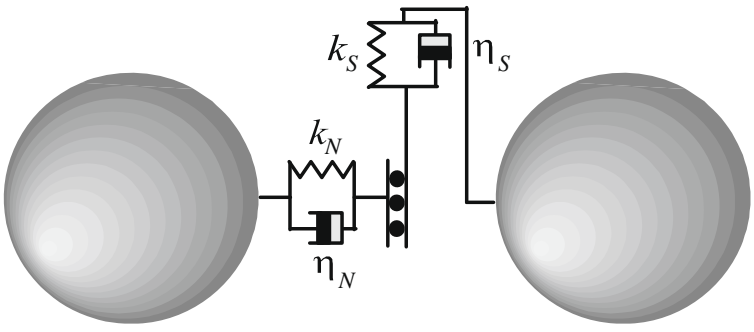

Fig. 4. Spring-dashpot-slider schematic for Cundall–Strack friction model between two colliding particles.

Here the time integral represents the angular displacement prior to torsional sliding. The expression (30) can be derived from (26) by integrating the friction stress $F_s/\pi a^2$ over the contact area with relative velocity $v_R = r\Omega_R$ oriented in the azimuthal direction, giving

$$M_t = \frac{2}{a^2}\int_0^a F_s(r) r^2 dr = -\frac{k_T a^2}{2}\int_{t_0}^{t} \Omega_T(\tau) d\tau - \frac{\eta_T a^2}{2}\Omega_T. \tag{31}$$

Comparing (30) and (31) yields the torsional stiffness and friction coefficients as

$$k_Q = k_T a^2/2, \quad \eta_Q = \eta_T a^2/2. \tag{32}$$

The particles will begin to spin relative to each other when the torque exceeds a critical value. The critical torque can be derived by integrating the moment $F_{crit} r/\pi a^2$ due to the critical sliding stress over the contact region, yielding

$$M_{t,crit} = \frac{2}{3} a F_{crit}. \tag{33}$$

When $|M_t| > M_{t,crit}$, the torsional resistance is given by

$$M_t = -M_{t,crit}\Omega_T/|\Omega_T|. \tag{34}$$

4.4. Rolling resistance

Several computational and experimental studies have pointed out that rolling, rather than slipping or twisting, is the primary micro-deformational mechanism in granular flows with small particle sizes [2,20,32]. Rolling is related to the change in position of the particle–particle contact point due to the particle rotation. The particles are simultaneously undergoing several different motions, including sliding, twist, and solid-body rotation of the particle aggregate, in addition to rolling, and there are several different ways that the rolling motion has been defined in the literature as distinct from these other motions. A discussion of four different definitions of rolling and of the effect of rolling motion on granular particle dynamics is given by Kuhn and Bagi [26].

An expression for the rolling displacement of arbitrary-shaped particles is derived by Bati and Kuhn [1] which is objective, such that the rolling velocity is independent of the reference frame in which it is measured. This property is important in part to ensure that the rolling motion is independent of solid-body rotation of the particle aggregate. Taking the rate of this expression and specializing to spherical particles yields an equation for the "rolling velocity" $\mathbf{v}_L$ of particle i as

$$\mathbf{v}_L = -R(\boldsymbol{\Omega}_i - \boldsymbol{\Omega}_j) \times \mathbf{n} - \frac{1}{2}\left(\frac{r_j - r_i}{r_j + r_i}\right)\mathbf{v}_S. \tag{35}$$

The first term is the velocity due to the difference in rotation rate of the particles projected onto the plane orthogonal to $\mathbf{n}$. The last term accounts for the effect of different particle size on rolling velocity. This definition reduces to that of Iwashita and Oda [20] when applied to a circular disk. We define the direction of rolling as $\mathbf{t}_R = \mathbf{v}_L/|\mathbf{v}_L|$, as shown in Fig. 5.

Following Iwashita and Oda [20], an expression for the rolling resistance torque M_r is postulated in the form of a rotational spring, dashpot, and slider system, as shown in Fig. 6, giving

$$M_r = -k_R\left(\int_{t_0}^{t} \mathbf{v}_L(\tau) d\tau\right) \cdot \mathbf{t}_R - \eta_R \mathbf{v}_L \cdot \mathbf{t}_R. \tag{36}$$

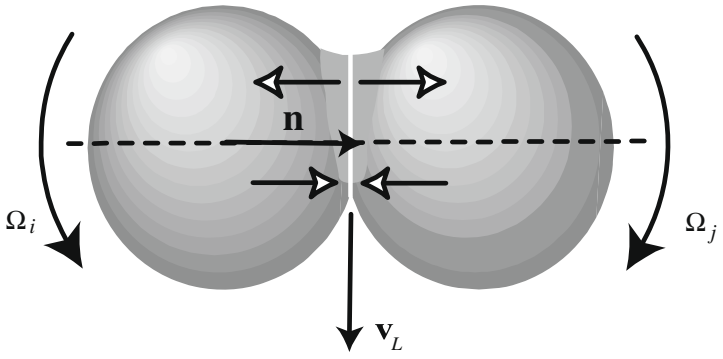

Fig. 5. Schematic showing asymmetry of the contact region between two spheres in a rolling motion in the presence of adhesive force. The dashed line passes through the particle centroids. The lines with the open arrows indicate the direction of normal particle motion during rolling.

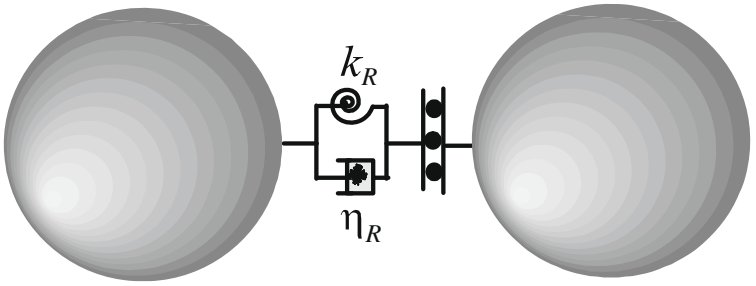

Fig. 6. Rotational spring-dashpot-slider system used for Iwashita-Oda rolling resistance torque model.

The first term on the right-hand side of (36) represents the spring force, where the time integral is the rolling displacement. The second term in (36) is a viscous resistance to rolling. The rolling torque is given by (36) for $|M_r|$ less than a critical value $M_{r,crit}$, beyond which $M_r = -M_{r,crit}$.

A number of different factors give rise to rolling resistance. Johnson [21] lists micro-slip, inelastic particle deformation, and surface irregularities all as possible contributing factors to rolling resistance in various situations. For spheres rolling on flat surfaces or on other spheres, Tabor [38] demonstrates that the rolling resistance primarily arises from elastic hysteresis. Iwashita and Oda [20] assume that the rolling stiffness and the sliding stiffness are of the same order of magnitude, or $k_{R0} = O(r_i k_T)$. Brilliantov and Pöschel [4] argue that rolling can be treated as a continuous series of normal displacements of the particle, as indicated schematically by the open arrows in Fig. 5. Based on this argument, they develop a model for rolling dissipation parameter using their model for normal dissipation coefficient of a viscoelastic material [5] which yields an expression for η_R of the form

$$\eta_R = \mu_R |F_{ne}|, \tag{37}$$

The rolling coefficient μ_R is related to the coefficient of restitution e by

$$\mu_R = \frac{1-e}{b w_0^{1/5} (K/m)^{2/5}}, \tag{38}$$

where the constant b is given by $b \cong 2.283$ and w_0 is a measure of the relative normal velocity between the particles prior to collision.

5. Modifications due to van der Waals Adhesion

Following the approach of Johnson et al. [22], we assume that van der Waals adhesive force acts only within the flattened contact region. The separation of the particles is further assumed to remain constant within this contact region, so that the adhesive force can be described using a surface potential γ, defined such that $2\pi\gamma a^2$ is the work that needs to be performed to separate the surfaces if the particles are treated as rigid bodies.

5.1. Normal force

For very slow particle impact velocities and with no fluid forces, the two particles approach an equilibrium state in which the elastic repulsion is balanced by the adhesive attraction of the particles. In this equilibrium state, the radius $a(t)$ of the contact region is given by

$$a_0 = \left(\frac{9\pi\gamma R^2}{E}\right)^{1/3}. \tag{39}$$

The expressions (19) and (20) for contact region radius and elastic rebound force F_{ne} are modified in the presence of van der Waals force, and can be written as [7,22]

$$\frac{F_{ne}}{F_C} = 4\left(\frac{a}{a_0}\right)^3 - 4\left(\frac{a}{a_0}\right)^{3/2} \tag{40}$$

and

$$\frac{\delta_N}{\delta_C} = 6^{1/3}\left[2\left(\frac{a}{a_0}\right)^2 - \frac{4}{3}\left(\frac{a}{a_0}\right)^{1/2}\right]. \tag{41}$$

In these equations, the critical force and overlap, F_C and δ_C, are given by

$$F_C = 3\pi\gamma R, \quad \delta_C = \frac{a_0^2}{2(6)^{1/3}R}. \tag{42}$$

The force F_{ne} is defined to be positive when it pushes the two particles toward each other. As the two particles move away from each other due to an applied stretching from the fluid or the particle inertial force, contact will be maintained even for negative values of δ_N via necking of the particle material (Fig. 3(b)), until the critical point is reached, at which $F_{ne} = -F_C$ and $\delta_N = -\delta_C$. As the particles are pulled further apart, the contact will suddenly break. To minimize the computational time, we pre-compute F_{ne}/F_C and a/a_0 as functions of δ_N/δ_C at the beginning of the calculation, and then use a look-up table to determine F_{ne} and $a(t)$ for the given value of δ_N at each time step. By writing k_N in terms of the contact region radius a in (21), rather than the more traditional form in terms of the overlap δ_N, we can use the same expressions (23) and (24) for the normal dissipation force as used for cases with no adhesion.

5.2. Sliding and twisting resistance

The effect of van der Waals adhesion on tangential sliding force was examined by Savkoor and Briggs [35], and a simplified model was proposed by Thornton [39] and Thornton and Yin [40]. Sliding is relatively rare for adhesive particles due to their small momentum, and it is of importance mainly in cases where an aggregate is torn apart by a fluid shear of by adhesion to another aggregate. To save computational time, we therefore adopt a simplified sliding resistance model proposed by Thorton [39], which was found to agree reasonably well with experimental data. This simplified approach uses the same expressions (25) and (28) that were developed for the case with no adhesive force, but replaces the critical sliding force by

$$F_{crit} = \mu_f |F_{ne} + 2F_C|, \tag{43}$$

where F_C is given in (42). The addition of the $2F_C$ term in (43) is necessary to ensure that the critical tangential force approaches $\mu_f F_C$ at the critical point when the particles are just about to separate. Similarly, the twisting resistance has the same form described in Section 4, but with the critical torque replaced by

$$M_{t,crit} = \frac{2}{3}\mu_f a |F_N + 2F_C|. \tag{44}$$

5.3. Rolling resistance

The van der Waals adhesion force leads to an additional mechanism for rolling resistance by inducing an asymmetry in the contact region, as shown in Fig. 5, due to the pulling apart of the particles surfaces on one side of the contact point and the pushing together of the particle surfaces on the other side. An expression for the torque induced by this adhesion-induced asymmetry is derived by Dominik and Tielens [12] as

$$M_r = -4F_C(a/a_0)^{3/2}\xi, \tag{45}$$

where ξ is the displacement of the particle centroid due to rolling in the $\mathbf{t}_R$ direction, given by the time integral in (31). Dominik and Tielens [12] further argue that the critical resistance occurs when the rolling displacement ξ achieves a critical value, corresponding to a critical rolling angle $\theta_{crit} = \xi_{crit}/R$. For $\xi > \xi_{crit}$, the rolling displacement ξ in (45) is replaced by ξ_{crit}.

6. Two particle collisions

We consider two particles located at time $t = 0$ at positions $x = \pm x_0$ and with velocities $dx/dt = \pm v_0$, such that the particles are traveling directly toward each other and not touching at the initial time. The particles have the same radius r_1 and elastic modulus E_1.

6.1. Normal collision with no adhesion

We initially assume that there are no adhesive or fluid forces acting between the particles. The particle position $\pm x(t)$ varies linearly in time as $x(t) = -x_0 + v_0 t$ until the particles collide with each other. Following collision, the particle inertia is resisted by the elastic and dissipative normal collision forces, giving an equation for the overlap $\delta \equiv \delta_N = 2(r_1 - x)$ as

$$\frac{d^2\delta}{dt^2} + 2\alpha\left(\frac{K}{m}\right)^{1/2}\delta^{1/4}\frac{d\delta}{dt} + 2\left(\frac{K}{m}\right)\delta^{3/2} = 0. \tag{46}$$

Defining a dimensionless time and overlap by

$$\hat{t} = t\left(r_1^{1/2}K/m\right)^{1/2}, \quad \hat{\delta} = \delta/r_1, \tag{47}$$

(46) becomes

$$\frac{d^2\hat{\delta}}{d\hat{t}^2} + 2\alpha\hat{\delta}^{1/4}\frac{d\hat{\delta}}{d\hat{t}} + 2\hat{\delta}^{3/2} = 0. \tag{48}$$

Eq. (48) is invariant to a transformation of the form

$$\delta^* = C\hat{\delta}, \quad t^* = \hat{t}/C^{1/4} \tag{49}$$

for any constant C. The collision rate w is defined by $w \equiv d\delta/dt$, such that applying (47) and (49) gives

$$w = (r_1^{5/2}K/m)^{1/2}\hat{w} = C^{-5/4}(r_1^{5/2}K/m)^{1/2}w^*. \tag{50}$$

If $w_0 \equiv w(0)$ is the initial collision rate, we can make $w^*(0) = 1$ in the transformed system by setting

$$C = r_1\left(\frac{K}{mw_0^2}\right)^{2/5}. \tag{51}$$

The coefficient of restitution e is defined as the ratio of the absolute value of the relative collision velocity after collision to that before collision, or

$$e \equiv |w_f/w_0| = |w_f^*|, \tag{52}$$

where subscripts 0 and f denote the values just before and just after the collision, respectively. The restitution coefficient e is therefore affected only by the coefficient α in (49), since all other coefficients in both the governing equation and the initial condition have been removed by scaling.

Eq. (48) is solved numerically using a fourth-order Runge–Kutta method with time step $\Delta t = 0.0001$. The solution for $\delta^*(t^*)$ is plotted in Fig. 7(a) for different values of the coefficient α. In each case, the overlap increases to some maximum value $\delta^* = \delta^*_{\max}$ at a time $t^* = t^*_{\max}$, and then decreases again to zero as the two particles rebound from each other. The scaled collision rate w^* is plotted for these same cases in Fig. 7(b). In Fig. 8, we plot the values of $\delta^*_{\max}$, $t^*_{\max}$ and $e = |w_f^*|$ as functions of α. To specify α for a given restitution coefficient e, we use a sixth-order polynomial fit the form

$$\alpha = 1.2728 - 4.2783e + 11.087e^2 - 22.348e^3 + 27.467e^4 - 18.022e^5 + 4.8218e^6. \tag{53}$$

For $\alpha > 1.2728$ the restitution coefficient is zero, and for $\alpha < 0.002$ the restitution coefficient is within 0.4% of unity.

6.2. Normal collision with van der Waals Adhesion

Adding adhesion force to the two particle normal collision problem, Eq. (48) for dimensionless particle overlap $\hat{\delta}$, defined in (47), reduces to the system

$$\frac{d^2\hat{\delta}}{d\hat{t}^2} + 2(2^{1/4})\alpha\hat{a}^{1/2}\frac{d\hat{\delta}}{d\hat{t}} + 4(2^{1/2})\hat{a}^3[1 - (\hat{a}_0/\hat{a})^{3/2}] = 0, \quad \hat{\delta} = 2\hat{a}^2\left[1 - \frac{2}{3}(\hat{a}_0/\hat{a})^{3/2}\right], \tag{54}$$

where $\hat{a} = a/r_1$ and $\hat{a}_0 = a_0/r_1$. Applying the transformation (49), with the transformation coefficient C given by (51) such that $w^*(0) = 1$ and letting $a^* = C^{1/2}\hat{a}$, the system (54) has the same form as given above with $\hat{a}_0$ replaced by the parameter a_0^*, defined by

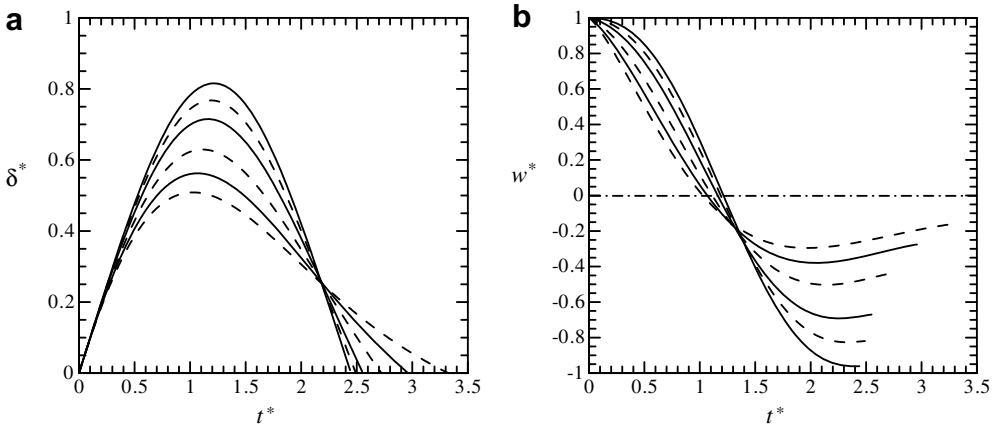

Fig. 7. Plots of (a) the dimensionless overlap δ^* and (b) the collision rate w^* as a function of time t^* with $\alpha = 0.02$ (solid), 0.1 (dashed), 0.2 (solid), 0.4 (dashed), 0.6 (solid), and 0.8 (dashed) (starting from the top).

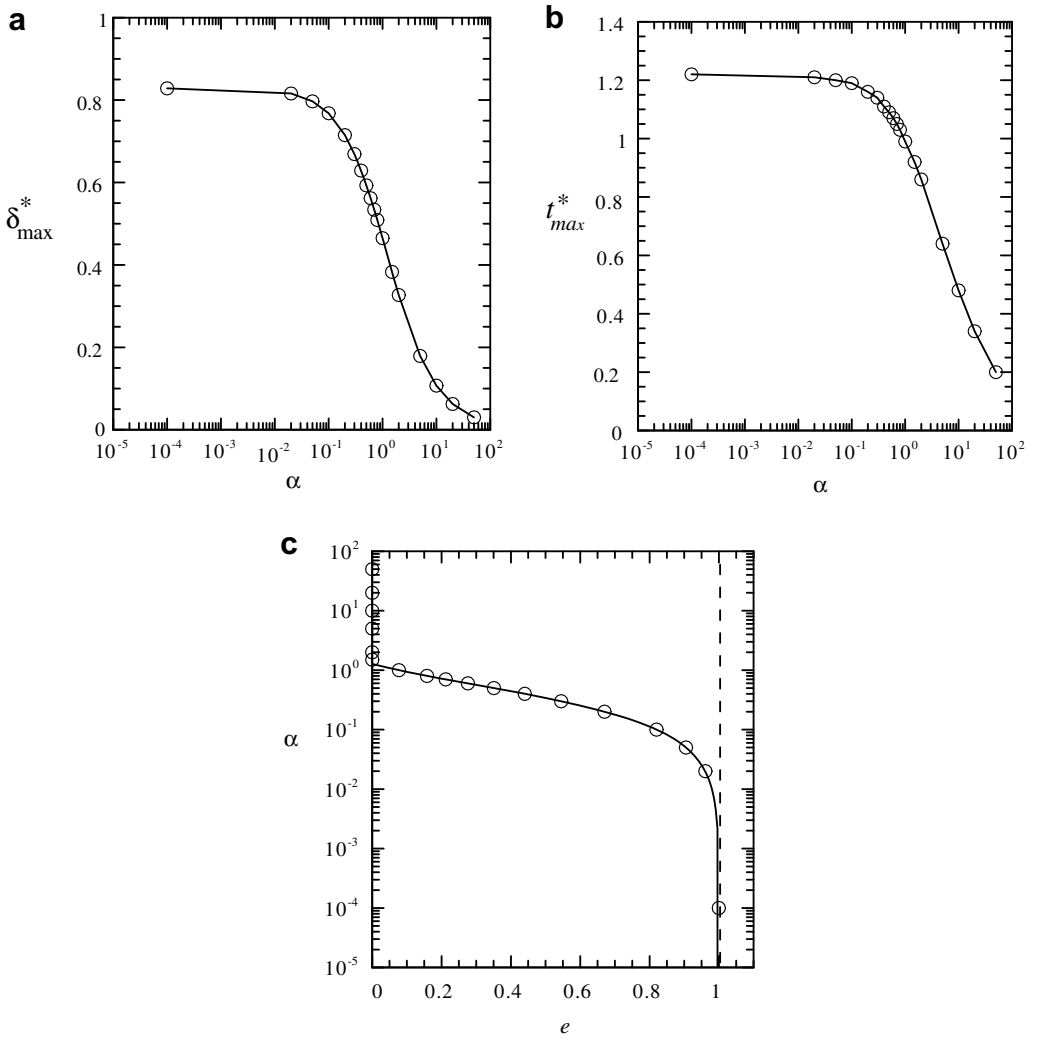

Fig. 8. Plots showing maximum dimensionless overlap δ^*_{max}, time t^*_{max} at which maximum is reached, and coefficient of restitution $e = \left|w^*_f\right|$ as functions of the damping coefficient α for two particle collisions. The solid curve in (c) is the polynomial curve fit in Eq. (53).

$$a^*_0 = \sqrt{2}\left(\frac{4ER^3}{3mw_0^2}\right)^{1/5}\left(\frac{9\pi\gamma}{8ER}\right)^{1/3}. \tag{55}$$

The only parameters in the system of equations for δ^* and a^* are the dissipation coefficient α and the parameter a^*_0. The equation for a^*_0 can be written in terms of two dimensionless parameters:

$$\lambda \equiv ER^3/mw_0^2, \quad \phi \equiv \gamma/ER. \tag{56}$$

The first parameter, λ, is a ratio of elastic rebound force to the particle inertia, and the second parameter, ϕ, is a ratio of attractive van der Waals force to elastic rebound force. In terms of these parameters, (55) becomes $a^*_0 \cong 2.28\lambda^{1/5}\phi^{1/3}$. A plot of the critical values of a^*_0 for the particles to stick together is given in Fig. 9 as a function of the dissipation coefficient α. For a^*_0 values greater than this critical value the particles will stick together with $a^* \to a^*_0$ at long time, whereas for a^*_0 less than this critical value the particles will rebound from each other and eventually separate.

7. Particle migration and aggregation in circular pipe flow

In this section, we demonstrate the performance of the discrete-element method by examining the behavior of particles advected in a circular pipe flow with a parabolic laminar velocity profile. The fluid velocity at the pipe center and the pipe radius are used for the velocity and length scales, U and L, of the flow. The computational domain has length $4L$ with periodic

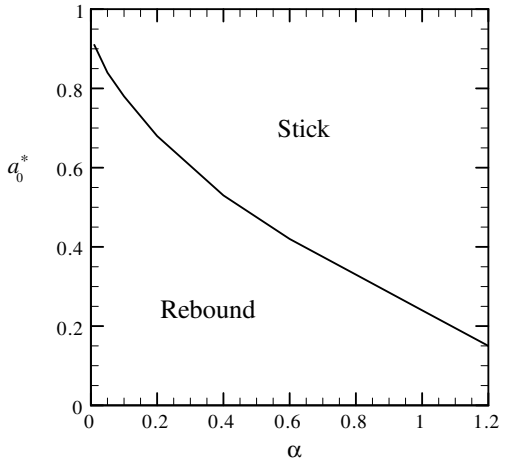

Fig. 9. Plot showing the critical value of the dimensionless equilibrium contact region radius a_0^* for which particles will stick together upon normal collision as a function of the dissipation parameter α.

boundary conditions at the two end planes. We use 5080 particles with effective radius $R/L = 0.01$, which are initially evenly distributed within the pipe. The particle velocities are initialized to be the same as the fluid velocity, along with a random perturbation with zero mean and maximum deviation equal to $0.5U$. The particle bulk concentration is $c_{bulk} = 0.01$, defined as the ratio of the volume of particles to the total volume. The ratio of fluid-to-particle phase density is $\chi = 0.01$, the pipe flow Reynolds number is $Re_F = UL/\nu = 3000$, the particle Stokes number is $St = 26.8$, and the particle elasticity parameter is $\lambda = 0.176$. The particle restitution coefficient is set as $e = 0.2$, corresponding to damping coefficient $\alpha = 0.72$. The flow is evolved using a fluid time step $U\Delta t/L = 0.1$, a particle time step $\Delta t_P = 0.0263\Delta t$, and a collision time step $\Delta t_C = 0.00026\ \Delta t$ over a time interval from $tU/L = (0,100)$. There are, therefore, 3838 collision time steps and 38 particle time steps for each fluid time step. The second-order Adams–Bashforth method is used for stepping the particles forward in time. Computations both with no adhesion and with van der Waals adhesion are reported. When performed on a standard Pentium 4 PC, the computation with no adhesion requires 45 min and that with van der Waals adhesion requires about 17 h. The greatly increased run time for the case with adhesive force is due to an increase in the number of particles that need to be evolved with the collision time step from about 50 for the case with no adhesion to up to 4500 for the case with adhesion.

Particle migration in pipe flow with no adhesion has been examined by a number of investigators, and two primary mechanisms have been identified that lead to lateral migration of particles. The first of these mechanisms is due-to-particle inertial effects, as incorporated in the lift and Magnus force terms discussed in Section 2 [18,36]. For a circular pipe flow, the inertial forces cause the particles to be depleted from the pipe center and walls and to tend to collect near the radial location $r/L = 0.6$. The second mechanism for particle lateral transport is the shear-induced migration that arises from particle–particle collisions in the presence of fluid shear. Leighton and Acrivos [27] showed that shear-induced migration causes particles to tend to migrate from regions of high to low particle concentration and from regions of high to low particle shear stress. Experimental studies of particle migration in a concentrated suspension are reported by Hampton et al. [15] and Han et al. [16] for flow in a circular tube and by Koh et al. [24] for flow in a rectangular channel. These investigations note that whereas the inertial force tends to concentrate particles in circular pipe flow midway between the pipe center and the wall, the particle–particle collision forces tend to make the particles more concentrated in the low shear region near the pipe center. For cases with small particle Reynolds number or high particle concentrations, the latter effect dominates and the particle concentrate peaks at the pipe center, whereas for cases with both large particle Reynolds numbers and low concentrations, a peak in particle concentration is observed near $r/L = 0.6$.

In computations with no adhesive force, the particle concentration field is averaged in both the axial and azimuthal directions. The particle concentration field is initially nearly uniform with radius (as shown by the dashed line in Fig. 10), but as the computations proceed the concentration becomes higher in a region near the pipe center spanning the radii $0.05 < r/L < 0.5$ and lower in the outer region spanning the radii $0.5 < r/L < 1$. An equilibrium configuration is approximately achieved by the final time, for which the concentration profile peaks to about $c = 0.03$ at $r/L = 0.2$ and decreases to about $c = 0.008$ at $r/L = 0.95$, before plunging to nearly zero at the wall. The concentration value at $r = 0$ tends to fluctuate significantly with time due to the small averaging volumes near the pipe center. The spatial fluctuations in Fig. 10 have typical radial length scale of about 0.1, which is roughly ten times the grid size used for determination of the concentration field. Comparison of computations performed both with and without the lift and Magnus forces indicate that the inertial forces have a small effect on the computational results. Similarly, computations with different values of the restitution coefficient and the elastic modulus indicate that the results are not sensitive to the values of these parameters.

The average number of particles involved in a collision ($\bar{n}_{CP}$) remains nearly constant at $\bar{n}_{CP} = 2.02 \pm 0.02$ during the computation, after a short initial transient. In Fig. 11, we plot the total number of particles involved in collisions (N_{CP}) and the

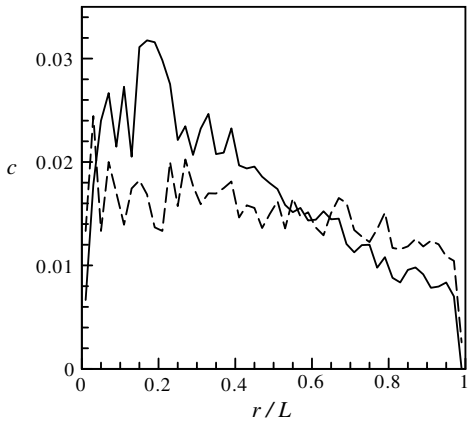

Fig. 10. Concentration profile at times $tU/L = 3$ (dashed line) and $tU/L = 100$ (solid line) for particle flow in a pipe with no adhesion force.

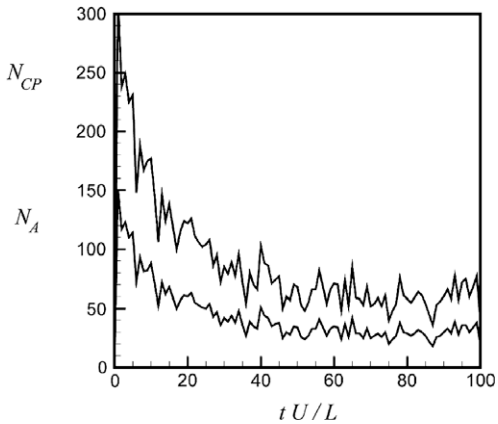

Fig. 11. Variation of the number of particles in aggregates (N_{CP}) and number of aggregates (N_A) with time for a case with no adhesion force.

number of distinct aggregates (N_A) formed from these colliding particles. Both of these measures exhibit a steady decline during the computation as the average relative velocity between the particles and the surrounding fluid decreases.

The same computation is now performed with the addition of van der Waals adhesion. Particle capture by surfaces was examined by Konstandopoulos [25] using a "frozen deposit" assumption coupled with a hard-sphere model for the particle collisions. While this assumption may be appropriate for examining particle impact on a wall with no bulk fluid flow, in the presence of a fluid flow bending and breakup of the wall-attached aggregates is important in regulating the particle capture process.

The current computations are performed with dimensionless adhesion parameter $\phi = 0.032$. The average number of particles in an aggregate, plotted in Fig. 12(a), is found to increase from about 2.2 early in the computation to about 5.5 by the end of the computation. The total number of particles involved in a collision (N_{CP}), plotted in Fig. 12(b), increases steadily during the computation, such that by $tU/L = 100$ approximately 80% of the particles are trapped in an aggregate. By contrast, the number of aggregates (N_A) quickly increases to about 700 and then remains fairly constant for the remainder of the computation. The aggregate growth occurs both by capture of individual particles by aggregates and by collision of aggregates with small number of particles to form larger aggregates. The distribution of particles within aggregates of different sizes can be determined by plotting the total number of particles $N_a(n_{PA})$ contained within aggregates of size n_{PA}, as shown in Fig. 13. Most aggregates have relatively few particles (less than 10), but some aggregates are found with up to 60 particles.

Particle concentration and axial velocity profiles are shown in Fig. 14 at a time $tU/L = 2$ near the start of the computation (dashed lines) and the final time ($tU/L = 100$). The particle concentration is initially approximately uniform across the pipe. As the computation progresses, the particle concentration is found to attain a nearly constant value in a broad central region $0 < r/L < 0.8$, which decreases gradually with time. The particle concentration increases rapidly within a near-wall region $0.8 < r/L < 1$, with a peak in particle concentration at approximately $r/L = 0.95$. The spike in particle concentration near the wall is an outcome of particles trapped in aggregates that are then captured by van der Waals adhesion to the wall. Unlike the case with no adhesion, the particles trapped at the pipe wall generally exhibit no forward motion due to the rolling

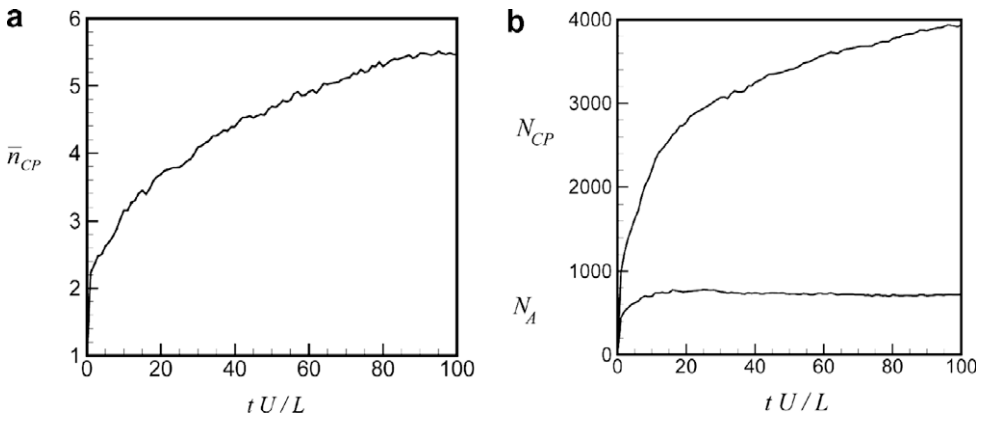

Fig. 12. For case with van der Waals adhesion force: (a) average number of particles per aggregate ($\bar{n}_{CP}$) vs time; (b) total number of particles in an aggregate (top) and number of aggregates (bottom) versus time.

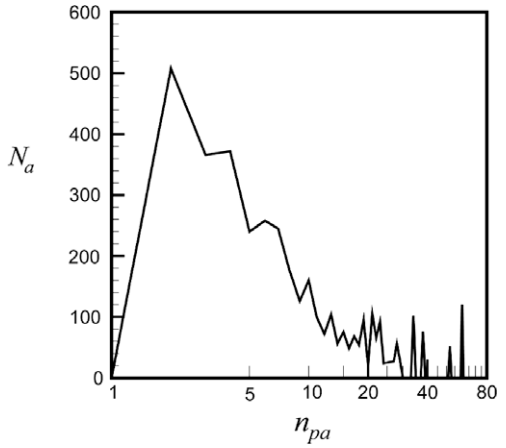

Fig. 13. Total number of particles N_a contained in aggregates with n_{PA} particles for the case with adhesive force at time $tU/L = 100$.

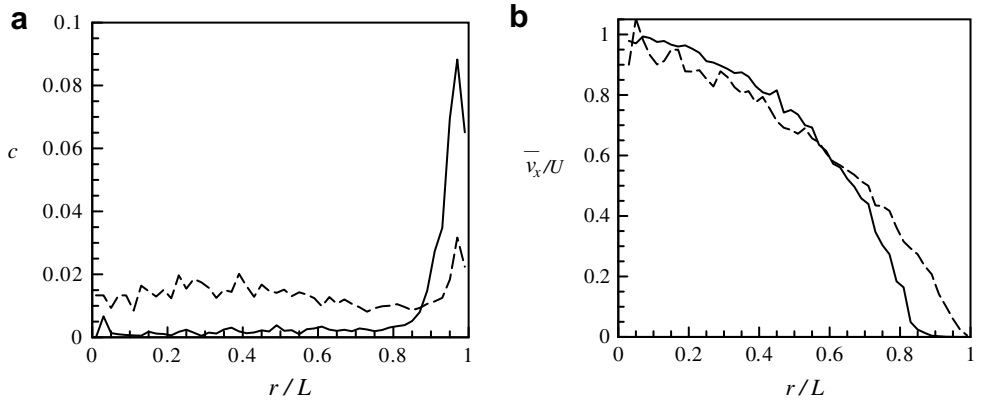

Fig. 14. Results for particle flow in a pipe with van der Waals adhesion force at times $tU/L = 2$ (dashed line) and $tU/L = 100$ (solid line): (a) concentration profile and (b) particle velocity profile.

resistance associated with the van der Waals adhesion, as given by (44). For instance, the average particle velocity is plotted as a function of radius in Fig. 14(b) for a time close to the start of the computation and for the final time. Near the start of the computation, the velocity profile approximately follows the parabolic profile of the fluid axial velocity, with some

fluctuations that grow more pronounced near the pipe center. As the particle collect on the walls, however, the axial velocity exhibits an increasing decline near the wall, such that by $tU/L = 100$ the particle axial velocity vanishes for r/L greater than about 0.85.

In order to clearly visualize the processes involved in aggregation formation in channel and pipe flow, we have performed a simulation for particle transport in a two-dimensional channel flow with van der Waals adhesion using the same parameter values as for the pipe flow computation reported above. A series of pictures showing the particle locations over a time sequence spanning an interval (0, 10) in tU/L from is given in Fig. 15. The particles are initially evenly spaced within the channel. Shortly after start of the computation, particles start colliding within the channel to form aggregates consisting of a small number of particles. These small aggregates collide with each other to form progressively larger aggregates. Some aggregates

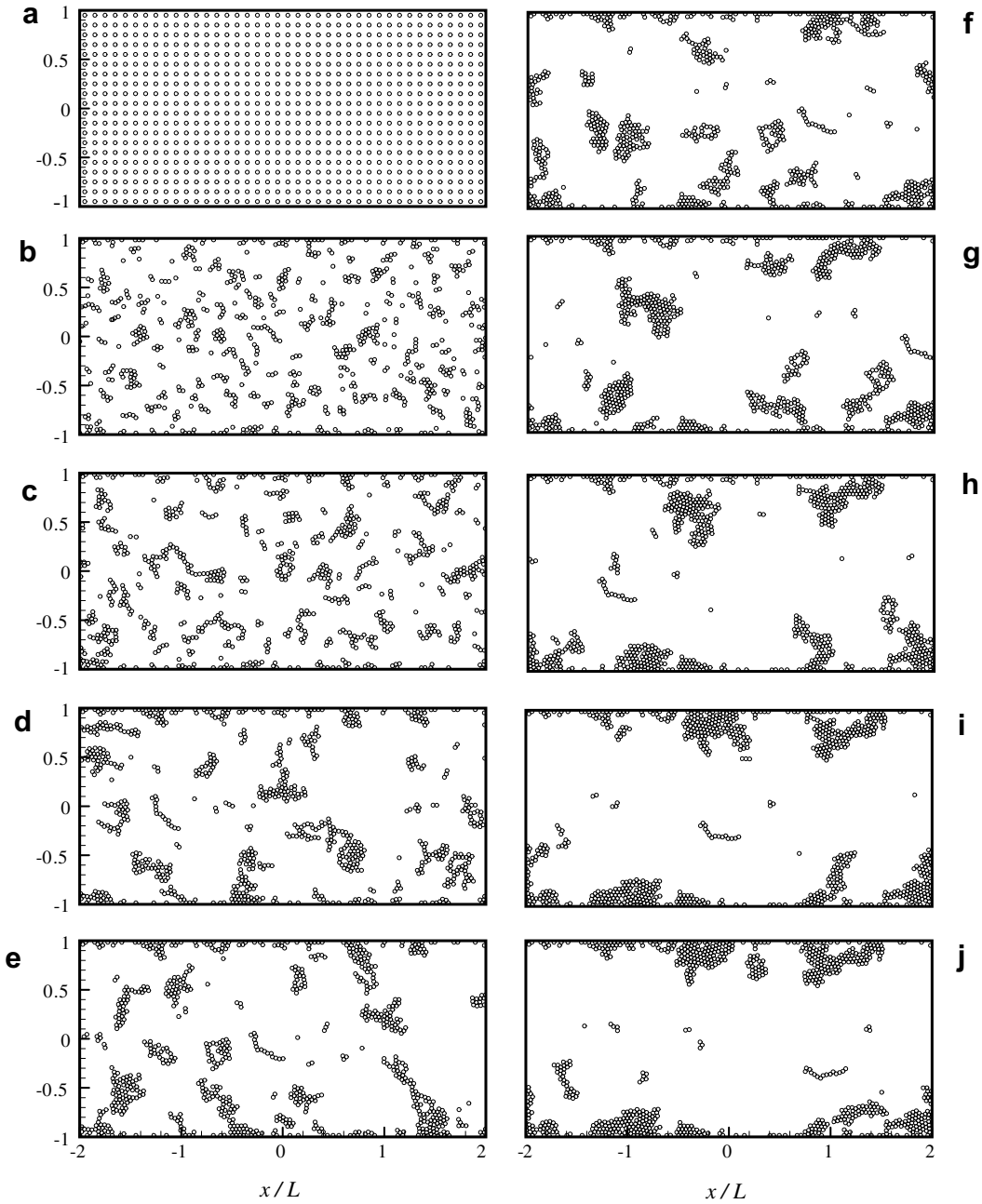

Fig. 15. Evolution of particle positions for a two-dimensional channel flow, showing development of aggregates and adhesion of aggregates to the channel walls due to van der Waals force, at times $tU/L = 0$ through 10.

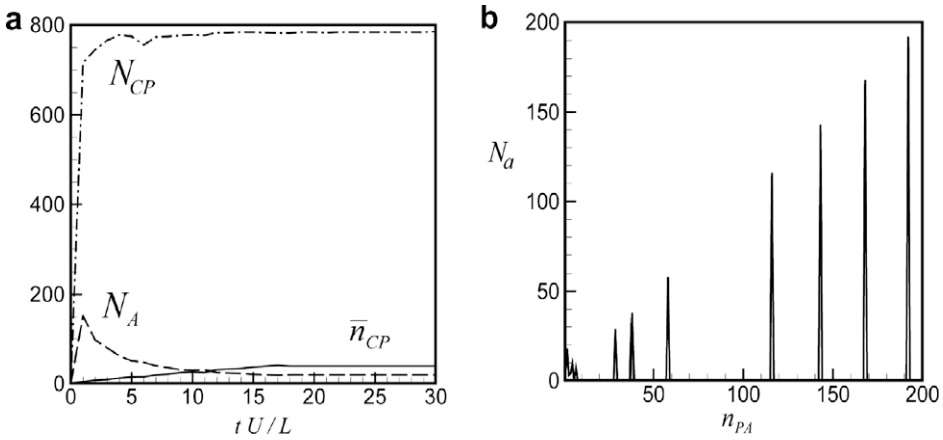

Fig. 16. Aggregation measures for two-dimensional channel flow with van der Waals adhesion: (a) time variation of total number of particles in an aggregate (N_{CP}), number of aggregates (N_A), and average number of particles in an aggregate ($\bar{n}_{CP}$); (b) number of particles N_a contained in aggregates of size n_{PA} at time $tU/L = 35$.

near the walls become attached to the walls, forming fingerlike projections sticking out into the flow. Some of these projecting aggregates break off due to the imposed shear, leaving a part attached to the wall and a part that returns to the flow. Other aggregates first project out into the flow and then bend via particle rolling to attach to the wall at several different positions. As the aggregates near the wall tumble due to the imposed shear, they capture other particles from the flow and transport them to the wall, such that by $tU/L = 10$ most of the particle are attached to the wall. As in the pipe flow case discussed previously, most of the particles contained in the aggregate layer lining the walls settle to a state with zero velocity, so that they become trapped at the wall.

Information on aggregate formation in two-dimensional channel flow are shown in Fig. 16. We observe that the total number of particles N_{CP} that are contained in an aggregate increases rapidly during the computation, and by $tU/L = 5$ includes nearly all particles. The number of aggregates increases in the very early part of the computation, peaks at about $tU/L = 1.2$, and then steadily decreases during the remainder of the computation as aggregates collide with one another to form fewer, larger aggregates. The average number of particles in an aggregate ($\bar{n}_{CP}$) increases throughout the computation. The number of particles contained in an aggregate of size n_{PA} is plotted in Fig. 16(b) at time $tU/L = 35$. We observe a distribution of aggregate sizes, ranging between aggregates with 2–5 particles to aggregates with nearly 200 particles.

8. Conclusions

A discrete-element method (DEM) is presented for simulation of particulate aerosols which includes particle–particle collisions and particle adhesion. The DEM is accelerated by implementation in the framework of a triple-time step algorithm, consisting of a fluid time step, a particle time step, and a collision time step. The particle collision model consists of terms for the normal elastic force on the particles, as well as forces and moments resisting particle sliding, rolling and twisting motions. Modifications to the collision forces and torques necessary to account for van der Waals adhesion are presented. Models for these forces and torques are designed based on a balance between desire to accurately describe the particle collision physics and desire to facilitate rapid computation with large numbers of particles in both two and three dimensions. Cases with normal collision of two particles are analyzed to develop the appropriate dimensionless parameters governing particle collision and the relationship between the normal force dissipation coefficient and the particle coefficient of restitution. The two particle collision cases are further used to examine conditions for two particle-to-stick or separate upon impact for different values of the restitution coefficient.

We demonstrate the capability of the method by examining both adhesive and non-adhesive particle transport in a pipe and channel flow. For the non-adhesive case, the particle concentration field is higher near the pipe center and lower near the walls due to the shear-induced migration effect, by which particle collisions in a shear flow cause particles to preferentially collect in regions of low shear rate. For the cases with adhesion, particles form aggregates within the volume of the flow which grow progressively larger as the aggregates collide with each other. A mechanism is described whereby aggregates form fingerlike projections attached at one end to the wall, which sweep out into the flow, capturing particles from with the main part of the flow and carrying them to the pipe wall. The fingerlike projects either break off or bend over to attach to the wall at several points, thereby becoming firmly bound to the wall. As time proceeds, nearly all of the particles become captured within these aggregates lining the wall. Because of the rolling resistance introduced by the van der Waals force, these wall-attached aggregates generally do not roll, but remain fixed in a thick layer lining the pipe wall.

The computational method described in this paper has been extended by the authors for other adhesion forces, including liquid bridging and receptor-ligand binding. It is desirable to extend the current computational model to apply to hydrosol flows, such as occur in nanoparticle suspensions, cohesive sediment transport problems, and various biological cell adhesion

and detachment problems. In order to extend the method to such problems, further research is necessary in order to develop a model that can account for the effects of fluid forces on the elastically deformed particles during particle collisions, while still retaining the high efficiency of the current computational method.

Acknowledgment

This research is supported by the University of Iowa Facilities Management Group (Mr. Ferman Minster, project manager) and by the Caterpillar Corporation (Youssef Dakhoul and Ron Dupree, project managers).

References

[1] K. Bagi, M.R. Kuhn, A definition of particle rolling in a granular assembly in terms of particle translations and rotations, Journal of Applied Mechanics 71 (2004) 493–501.
[2] J.P. Bardet, Observations on the effects of particle rotations on the failure of idealized granular materials, Mechanics of Materials 18 (2) (1994) 159–182.
[3] G. Barnocky, R.H. Davis, The influence of pressure-dependent density and viscosity on the elastohydrodynamic collision and rebound of two spheres, Journal of Fluid Mechanics 209 (1989) 501–519.
[4] N.V. Brilliantov, T. Pöschel, Rolling as a 'continuing collision', European Physics Journal B 12 (1999) 299–301.
[5] N.V. Brilliantov, F. Spahn, J.-M. Hertzsch, T. Pöschel, Model for collisions in granular gases, Physical Review E 53 (5) (1996) 5382–5392.
[6] A.B. Burd, G.A. Jackson, Modeling steady-state particle size spectra, Environmental Science and Technology 36 (2002) 323–327.
[7] A. Chokshi, A.G.G.M. Tielens, D. Hollenbach, Dust coagulation, Astrophysical Journal 407 (1993) 806–819.
[8] P.W. Cleary, G. Metcalfe, K. Liffman, How well do discrete element granular flow models capture the essentials of mixing processes?, Applied Mathematical Modeling 22 (1998) 995–1008
[9] C.T. Crowe, M. Sommerfeld, Y. Tsuji, Multiphase Flows with Droplets and Particles, CRC Press, Boca Raton, 1998.
[10] P.A. Cundall, O.D.L. Strack, A discrete numerical model for granular assembles, Geotechnique 29 (1) (1979) 47–65.
[11] R. Di Felice, The voidage function for fluid–particle interaction systems, International Journal of Multiphase Flow 20 (1994) 153–159.
[12] C. Dominik, A.G.G.M. Tielens, Resistance to rolling in the adhesive contact of two elastic spheres, Philosophical Magazine A 92 (3) (1995) 783–803.
[13] C. Dominik, A.G.G.M. Tielens, The physics of dust coagulation and the structure of dust aggregates in space, Astrophysical Journal 480 (1997) 647–673.
[14] O.A. Druzhinin, L.A. Ostrovsky, The influence of Basset force on particle dynamics in two-dimensional flows, Physica D 76 (1994) 34–43.
[15] R.E. Hampton, A.A. Mammoli, A.L. Graham, N. Tetlow, S.A. Altobelli, Migration of particles undergoing pressure-driven flow in a circular conduit, Journal of Rheology 41 (1997) 621–640.
[16] M. Han, C. Kim, M. Kim, S. Lee, Particle migration in tube flow of suspensions, Journal of Rheology 43 (5) (1999) 1157–1174.
[17] H. Hertz, Über die Berührung fester elastische Körper, Journal of Reine und Angewandte Mathematik 92 (1882) 156–171.
[18] B.P. Ho, L.G. Leal, Inertial migration of rigid spheres in two-dimensional unidirectional flows, Journal of Fluid Mechanics 65 (1974) 365–400.
[19] K.C. Hu, R. Mei, Particle collision rate in fluid flows, Physics of Fluids 10 (4) (1998) 1028–1030.
[20] K. Iwashita, M. Oda, Rolling resistance at contacts in simulation of shear band development by DEM, Journal of Engineering Mechanics 124 (3) (1998) 285–292.
[21] K.L. Johnson, Contact Mechanics, Cambridge University Press, Cambridge, UK, 1985.
[22] K.L. Johnson, K. Kendall, A.D. Roberts, Surface energy and the contact of elastic solids, Proceedings of the Royal Society of London A 324 (1971) 301–313.
[23] H. Kim, H. Arastoopour, Extension of kinetic theory to cohesive particle flow, Powder Technology 122 (2002) 83–94.
[24] C.J. Koh, P. Hookham, L.G. Leal, An experimental investigation of concentrated suspension flows in a rectangular channel, Journal of Fluid Mechanics 266 (1994) 1–32.
[25] A. Konstandopoulos, Deposit growth dynamics: particle sticking and scattering phenomena, Powder Technology 109 (2000) 262–277.
[26] M.R. Kuhn, K. Bagi, Contact rolling and deformation in granular media, International Journal of Solids and Structures 41 (2004) 5793–5820.
[27] D. Leighton, A. Acrivos, The shear-induced migration of particles in concentrated suspensions, Journal of Fluid Mechanics 181 (1987) 415–439.
[28] L. Mädler, Liquid-fed aerosol reactors for one-step synthesis of nano-structured particles, KONA 22 (2004) 107–120.
[29] J.S. Marshall, Particle dispersion in a turbulent vortex core, Physics of Fluids 17 (2) (2005). 025104-1–025104-15.
[30] T. Mikami, H. Kamiya, M. Horio, Numerical simulation of cohesive powder behavior in a fluidized bed, Chemical Engineering Science 53 (10) (1998) 1927–1940.
[31] R.D. Mindlin, Compliance of elastic bodies in contact, Journal of Applied Mechanics 16 (1949) 259–268.
[32] M. Oda, J. Konishi, S. Nemat-Nasser, Experimental micromechanical evaluation of strength of granular materials: effects of particle rolling, Mechanics of Materials 1 (4) (1982) 269–283.
[33] P.G. Saffman, The lift on a small sphere in a slow shear flow, Journal of Fluid Mechanics 22 (1965) 385–400.
[34] P.G. Saffman, Corrigendum to 'The lift force on a small sphere in a slow shear flow', Journal of Fluid Mechanics 31 (1968) 624.
[35] A.R. Savkoor, G.A.D. Briggs, The effect of tangential force on the contact of elastic solids in adhesion, Proceedings of the Royal Society of London A 356 (1977) 103–114.
[36] G. Segre, A. Silberberg, Behavior of macroscopic rigid spheres in Poiseuille flow. Part 2. Experimental results and interpretation, Journal of Fluid Mechanics 14 (1962) 136–157.
[37] M.V. Smoluchowski, Versuch einer mathematischen theorie der koagulationskinetic kolloder losunggen, Zeitschrift of Physics and Chemistry 92 (1917) 129.
[38] D. Tabor, The mechanism of rolling friction: the elastic range, Proceedings of the Royal Society of London A 229 (1955) 198–220.
[39] C. Thornton, Interparticle sliding in the presence of adhesion, Journal Physics D: Applied Physics 24 (1991) 1942–1946.
[40] C. Thornton, K.K. Yin, Impact of elastic spheres with and without adhesion, Powder Technology 65 (1991) 153–166.
[41] Y. Tsuji, T. Tanaka, T. Ishida, Lagrangian numerical simulation of plug flow of cohesionless particles in a horizontal pipe, Powder Technology 71 (1992) 239–250.
[42] J. Visser, Van der Waals and other cohesive forces affecting powder fluidization, Powder Technology 58 (1989) 1–10.
[43] M.W. Weber, D.K. Hoffman, C.M. Hrenya, Discrete-particle simulations of cohesive granular flow using a square-well potential, Granular Matter 6 (2004) 239–254.
[44] J.J. Zhang, X.Y. Li, Modeling particle-size distribution dynamics in a flocculation system, AIChE Journal 49 (7) (2003) 1870–1882.